**RESEARCH ARTICLE**

Check for updates

# High-performance Rh@MgO catalysts for complete dehydrogenation of hydrazine borane: a comparative study†

Ahmet Bulut,[a] Mustafa Erkartal, [ID] *[b] Mehmet Yurderi,[c,d] Tuba Top[e] and Mehmet Zahmakiran*[a]

Hydrazine borane (HB) has great potential as a safe and convenient hydrogen carrier material due to its high hydrogen capacity (15.4 wt%) and good stability under ambient conditions. However, efficient hydrogen production through complete decomposition of hydrazine borane at low temperatures (<373 K) constitutes a major challenge. Herein, we report the successful immobilization of monodisperse Rh nanoparticles on MgO solid support, leading to the formation of the Rh@MgO catalyst. This developed catalyst exhibits outstanding catalytic performance in the dehydrogenation of HB, achieving a remarkable turnover frequency (TOF) of 2005.34 h$^{-1}$ at 50 °C with 100% H$_2$ selectivity, despite containing only 2 wt% Rh. Comparative experiments with Rh on various metal–oxide nanoparticles, other transition metal catalysts on MgO, and Ni grown on MgO in both single-phase and bimetallic forms reveal that Rh@MgO consistently outperforms these alternatives. The exceptional catalytic activity is attributed to the synergistic interaction between Rh and MgO, which involves several key factors: the homogeneous dispersion of ultrafine, monodisperse Rh particles enhances catalytic efficiency; the proximity of the work functions of Rh and MgO results in a low-energy Schottky barrier that facilitates electron transfer; and the localization of electrons in surface defects of MgO aligns with the Fermi level of Rh, further promoting electron transfer through Fermi level pinning (FLP). The combination of low Rh content and cost-effective MgO support presents a promising pathway for both laboratory-scale research and practical industrial applications, highlighting the potential of the Rh@MgO catalyst as an efficient and economically viable solution for catalytic processes.
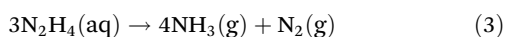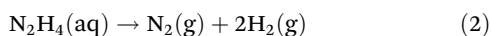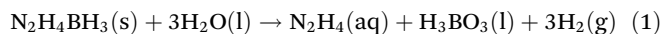
## 1. Introduction

Today, the majority of global energy demand is met by burning fossil fuels, which releases significant amounts of greenhouse gases into the environment, contributing to global warming.[1,2] In this context, hydrogen gas (H$_2$) is recognized as a clean energy vector that can address global energy problems and reduce environmental pollution caused by fossil fuel use due to its abun-

*[a]Department of Biotechnology, Faculty of Science, Bartin University, 74100 Bartin, Türkiye. E-mail: mzahmakiran@bartin.edu.tr*

*[b]Department of Basic Sciences, Faculty of Engineering, Architecture and Design, Bartin University, 74100 Bartin, Türkiye. E-mail: merkartal@bartin.edu.tr*

*[c]Department of Electronics and Automation, Bartın Vocational School, Bartın University, 74100 Bartın, Türkiye*

*[d]Central Research Laboratory, Research & Application Center, Bartın University, 74100 Bartın, Türkiye*

*[e]Department of Chemistry, Faculty of Science, Karabük University, 78000 Karabük, Türkiye*

†Electronic supplementary information (ESI) available. See DOI: https://doi.org/10.1039/d4qi02575j

dance, clean-burning properties, and high energy intensity (142 MJ kg$^{-1}$). However, the low density and explosive nature of H$_2$ make it difficult to store and transport in compressed form, presenting a major challenge to its growing popularity as an energy carrier.[3–7] Among various hydrogen storage solutions, chemical hydrogen storage materials have garnered significant attention due to their high gravimetric/volumetric capacity for hydrogen storage and safety compared to physical hydrogen storage.[8–13]

Hydrazine borane (N$_2$H$_4$BH$_3$) has garnered attention as a promising chemical hydrogen storage material due to its high volumetric hydrogen capacity of 15.4 wt% and its safe storage and transportation characteristics. The compound can be completely converted into hydrogen through a series of dehydrogenation reactions.[14,15] Specifically, the BH$_3$ group undergoes hydrolysis, yielding boric acid and hydrogen (eqn (1)), while the N$_2$H$_4$ moiety decomposes to produce nitrogen gas and hydrogen (eqn (2)) and can also decompose further to produce ammonia and nitrogen (eqn (3)). The overall process theoretically allows one mole of N$_2$H$_4$BH$_3$ to produce five moles of hydrogen and one mole of nitrogen. This results in a gravi-

**342** | *Inorg. Chem. Front.*, 2025, **12**, 342–354

This journal is © the Partner Organisations 2025

metric hydrogen storage capacity (GHSC) for the $N_2H_4BH_3$–$3H_2O$ system of 10.0 wt%, which is superior to that of other hydrogen storage materials such as $NaBH_4$–$4H_2O$ (7.3 wt%) and $NH_3BH_3$–$4H_2O$ (5.9 wt%). Despite the efficient hydrolysis of the $BH_3$ group, the decomposition of the $N_2H_4$ component is relatively slow, even with catalysts, and may produce undesired ammonia.[16–18]

$$N_2H_4BH_3(s) + 3H_2O(l) \rightarrow N_2H_4(aq) + H_3BO_3(l) + 3H_2(g) \quad (1)$$

$$N_2H_4(aq) \rightarrow N_2(g) + 2H_2(g) \quad (2)$$

$$3N_2H_4(aq) \rightarrow 4NH_3(g) + N_2(g) \quad (3)$$

A wide range of metal-based nanocatalysts have been explored for hydrogen generation from the decomposition of hydrazine borane (HB),[18–22] with particular focus on catalysts containing platinum group metals such as Pt,[15,20,23–25] Rh,[26,27] and Ru.[28–30] These catalysts are known for their exceptional efficiency in hydrogen production, even at very low metal concentrations. Despite the scarcity and high cost associated with platinum group metals, their use as catalysts in HB decomposition remains highly significant due to their unparalleled catalytic performance.[31,32] Recently, nano-metal particles have garnered considerable attention for their unique properties that differ from those of their bulk counterparts. However, these nanoparticles (NPs) are prone to aggregation due to their high surface energy, which can diminish their active surface area and reduce the availability of catalytic sites.[33,34] To enhance the stability of metal NPs, various strategies have been employed, including the use of surfactants or the incorporation of support materials with large specific surface areas, including MOFs,[35–37] zeolites,[38] and metal oxides.[39]

Magnesium oxide (MgO) has recently emerged as a highly effective support material for heterogeneous catalysis, attracting attention due to its unique properties, such as its large surface area, basicity, and crystal structure.[40,41] These characteristics make MgO particularly suitable for enhancing the dispersion and stability of metal nanoparticles (NPs), which are crucial for maintaining high catalytic activity.[42–44] In the context of hydrogen production from hydrazine borane (HB), the basic sites of MgO play a pivotal role in promoting dehydrogenation by facilitating the cleavage of N–H bonds, thereby improving the selectivity towards hydrogen and nitrogen formation. Hence, immobilizing metal nanoparticles on an MgO support may enhance the catalytic performance in the dehydrogenation of HB. Based on this motivation, we addressed herein a facile synthesis of rhodium nanoparticles supported on MgO, which will hereafter be referred to as Rh/MgO, and their superior catalysis for the complete dehydrogenation of HB. To this end, the Rh/MgO catalyst was simply and reproducibly prepared using the surfactant-free deposition-reduction technique.[45] The resulting Rh/MgO catalyst was characterized by using a combination of multipronged techniques including inductively coupled plasma optical emission spectroscopy (ICP-OES), powder X-ray diffraction (PXRD), X-ray photoelectron spectroscopy (XPS), field-emission scanning electron

microscopy (FE-SEM), and transmission electron microscopy (TEM) analyses. The catalytic performance of Rh/MgO in terms of activity, selectivity and stability has been tested in the catalytic decomposition of HB under air at 323 K. It was found that the Rh/MgO catalyst exhibits a record catalytic activity in the complete dehydrogenation of HB featuring an initial turnover frequency (TOF) value of 2005.34 $h^{-1}$ at 323 K, which is the highest TOF value among all heterogeneous catalysts reported to date for this reaction (vide infra). To the best of our knowledge, Rh/MgO is the first example of a monometallic catalyst that achieves complete decomposition of HB with 100% dehydrogenation selectivity under mild conditions.

## 2. Materials and methods

### 2.1. Materials

Rhodium(III) chloride hydrate ($RhCl_3 \cdot 3H_2O$), magnesium oxide (MgO), titanium dioxide ($TiO_2$), cerium dioxide ($CeO_2$), zirconium dioxide ($ZrO_2$), aluminum oxide ($Al_2O_3$), hydrotalcite (HTaL), ethanol ($C_2H_5OH$), hydrazine hemisulfate ($H_2NNH_2 \cdot 0.5H_2SO_4$), sodium borohydride ($NaBH_4$), dioxane ($C_4H_8O_2$) and $n$-pentane ($C_5H_{12}$) were purchased from Sigma-Aldrich®. Hydrazine borane ($N_2H_4BH_3$) was synthesized by following previously reported protocols. Deionized water was distilled using a water purification system (the Milli-Q water purification system). All chemicals were used as received and without further purification.

### 2.2. Characterization

Rhodium (Rh) contents of the sample were determined by ICP-OES (PerkinElmer DRC II model) after each sample was completely dissolved in a mixture of $HNO_3/HCl$ (v/v = 1/3). Powder X-ray diffraction (PXRD) patterns were recorded with a Rigaku Ultima IV diffractometer using Cu-Kα radiation (wavelength 1.54 Å, 40 kV, 55 mA). SEM analyses were conducted by using the Quanta 400F field emission SEM. The EDS system and the Inca software were exploited to acquire and process SEM-EDS data. A TEM sample was prepared by dropwise addition of the a dilute catalyst suspension on a copper-coated carbon TEM grid followed by the evaporation of the solvent. Conventional TEM measurements were carried out on a JEOL JEM-200 CX transmission electron microscope operating at 120 kV. XPS measurements were performed via a Physical Electronics 5800 XP spectrometer equipped with a hemispherical analyzer and a monochromatic Al-Kα X-ray source (1486.6 eV, 15 kV, and 350 W, with a pass energy of 23.5 eV). Gas adsorption/desorption isotherms were obtained by using a Micromeritics Tristar II Plus surface area and pore size analyzer.

### 2.3. Preparation of Rh/MgO

The Rh/MgO catalyst was prepared by using a surfactant-free deposition-reduction technique.[45] In a typical experiment, 5.0 mL of an aqueous solution containing $RhCl_3 \cdot 3H_2O$ (13.52 mg, 0.06 mmol) and solid support (100 mg of MgO) was mixed for 3 h. Then, fresh aqueous $NaBH_4$ solution (1.0 mL,

This journal is © the Partner Organisations 2025

Inorg. Chem. Front., 2025, 12, 342–354 | 343

11 mg, 0.30 mmol) was added to this mixture and the resulting solution was stirred for half an hour under ambient conditions. After centrifugation (6000 rpm, 5 min), copious washing with water (3 × 20 mL), filtration, and drying in a vacuum oven at 373 K and $10^{-2}$ Torr, Rh/MgO was obtained as a gray powder.

### 2.4. Testing the catalytic activity of Rh/MgO in the dehydrogenation of hydrazine borane

The catalytic activity of Rh@MgO in the dehydrogenation of HB was determined by volumetric measurement of the rate of gas evolution. The volume of released gas during the reaction was monitored using a gas burette through water displacement.[46] Before starting the catalytic activity tests, a jacketed one-necked reaction flask (50.0 mL) containing a Teflon-coated stirring bar was placed on a magnetic stirrer (Heidolph MR-3004) whose temperature was adjusted by circulating water through its jacket from a constant temperature bath. In a typical catalytic activity test, the Rh@MgO catalyst was weighed and transferred into the reaction flask, and then 9.5 mL of $H_2O$ was added into the reaction flask followed by rigorous stirring for 15 min to achieve thermal equilibrium. Next, 0.5 mL of aqueous HB solution was added into the reaction flask via its septum using a 1.0 mL gastight syringe, and the catalytic reaction was started ($t = 0$ min) by stirring the mixture at 900 rpm and 323 K. Gaseous products were first passed through the HCl (0.1 M) trap to ensure $NH_3$ absorption. The volume of the remaining $H_2$ along with that of $N_2$ was monitored using the gas burette through water displacement. Then, the molar ratio ($\lambda$) was calculated as $\lambda = n(H_2 + N_2)/n(N_2H_4BH_3)$ by the total volume of $H_2$ and $N_2$. Hydrogen selectivity ($\alpha$) for $N_2H_4BH_3$ dehydrogenation ($N_2H_4BH_3 + 3H_2O \rightarrow B(OH)_3 + (3 + 2\alpha)H_2 + (2\alpha + 1)/3N_2 + 4(1 - \alpha)/3NH_3$) was obtained by using the following equation:[47]

$$\alpha = \frac{3\lambda - 10}{8} \left[ \lambda = \frac{n[H_2 + N_2]}{n[N_2H_4BH_3]} \left( \frac{10}{3} \leq \lambda \leq 6 \right) \right]$$

The catalytic durability of the Rh@MgO catalyst in HB dehydrogenation was evaluated by recyclability experiments. The recyclability of Rh@MgO in the dehydrogenation of HB was determined by performing a series of experiments started with an aqueous HB solution at 323 K. Immediately after HB conversion was achieved in the 1st catalytic run, another equivalent amount of fresh HB was added to the reaction mixture, leading to more gas formation, which demonstrated the reusability of the catalyst.

## 3. Results and discussion

### 3.1 Catalyst characterization

The Rh@MgO catalyst was synthesized using a surfactant-free deposition-reduction method.[45] In a typical experiment, 5.0 mL of an aqueous solution containing $RhCl_3 \cdot 3H_2O$ (13.52 mg, 0.06 mmol) was mixed with 100 mg of MgO solid support and stirred for 3 hours. Subsequently, a fresh aqueous

solution of $NaBH_4$ (1.0 mL, 11 mg, 0.30 mmol) was added to the mixture and stirred for 30 minutes under ambient conditions. The resulting solution was then centrifuged (5 min, 6000 rpm), followed by thorough washing with water and ethanol (three times, 20 mL each). The solid was filtered and dried at 373 K under vacuum ($10^{-2}$ Torr) in an oven, yielding Rh@MgO as a gray powder (Fig. 1a). Composite catalysts were prepared with initial Rh loadings of 1, 2, 4, and 8 wt%. Based on the catalytic performance results (discussed below) and the high cost of rhodium, further experiments were conducted using Rh@MgO with 2 wt% Rh. Consequently, the structural characterization presented below focuses on this catalyst composition.

The Rh@MgO catalyst was characterized using various microscopic and spectroscopic techniques to elucidate its morphology, particle size distribution, and elemental composition. The SEM images (Fig. 1b) reveal the surface morphology of the Rh@MgO catalyst. The micrographs demonstrate uniform distribution of particles on the MgO support, with no significant agglomeration, indicating successful dispersion of the Rh nanoparticles across the MgO surface. Further insights into the particle size and distribution of the Rh nanoparticles were obtained using TEM analysis (Fig. 1c). The TEM images reveal well-dispersed Rh nanoparticles with a narrow size distribution. The average particle size of the Rh nanoparticles, measured from the TEM images, was found to be approximately 2.55 nm, indicating the effectiveness of the synthesis method in controlling nanoparticle size (Fig. 1f). The SEM-EDX elemental maps illustrate a homogeneous distribution of Rh throughout the MgO matrix, verifying that the Rh nanoparticles are evenly dispersed and attached on the MgO support (Fig. 1d). The Rh content in Rh@MgO, calculated as 1.65 wt% from elemental mapping and 1.54 wt% from ICP-OES analysis, shows good agreement with each other and with the initial 2 wt% Rh added during the synthesis.

The crystalline structure of the Rh@MgO catalyst was investigated using PXRD, as shown in Fig. 2a. The diffraction pattern exhibits characteristic peaks corresponding to the MgO phase being rock salt structured and crystallized in the cubic $Fm\bar{3}m$ space group.[48] No additional peaks corresponding to Rh metal or Rh oxides are observed, suggesting that the Rh nanoparticles are either of very low concentration or well-dispersed on the MgO surface, making them undetectable by PXRD. The surface composition and chemical state of the elements present in the Rh@MgO catalyst were examined using XPS. The survey spectrum in Fig. 2b shows peaks corresponding to Mg, O, and Rh, indicating the presence of these elements on the catalyst surface. The lack of notable peaks from other impurities indicates that the Rh@MgO catalyst is highly pure. The Rh peak further confirms the successful deposition of Rh onto the MgO support, while the strong Mg and O peaks correspond to the underlying MgO structure. High-resolution XPS spectra of the Rh (3d) region, presented in Fig. 2c, provide insights into the oxidation state of Rh in the Rh@MgO catalyst. The Rh (3d) spectrum reveals two distinct peaks at binding energies of 306.2 and 311.1 eV, corres-

**344** | *Inorg. Chem. Front.*, 2025, **12**, 342–354

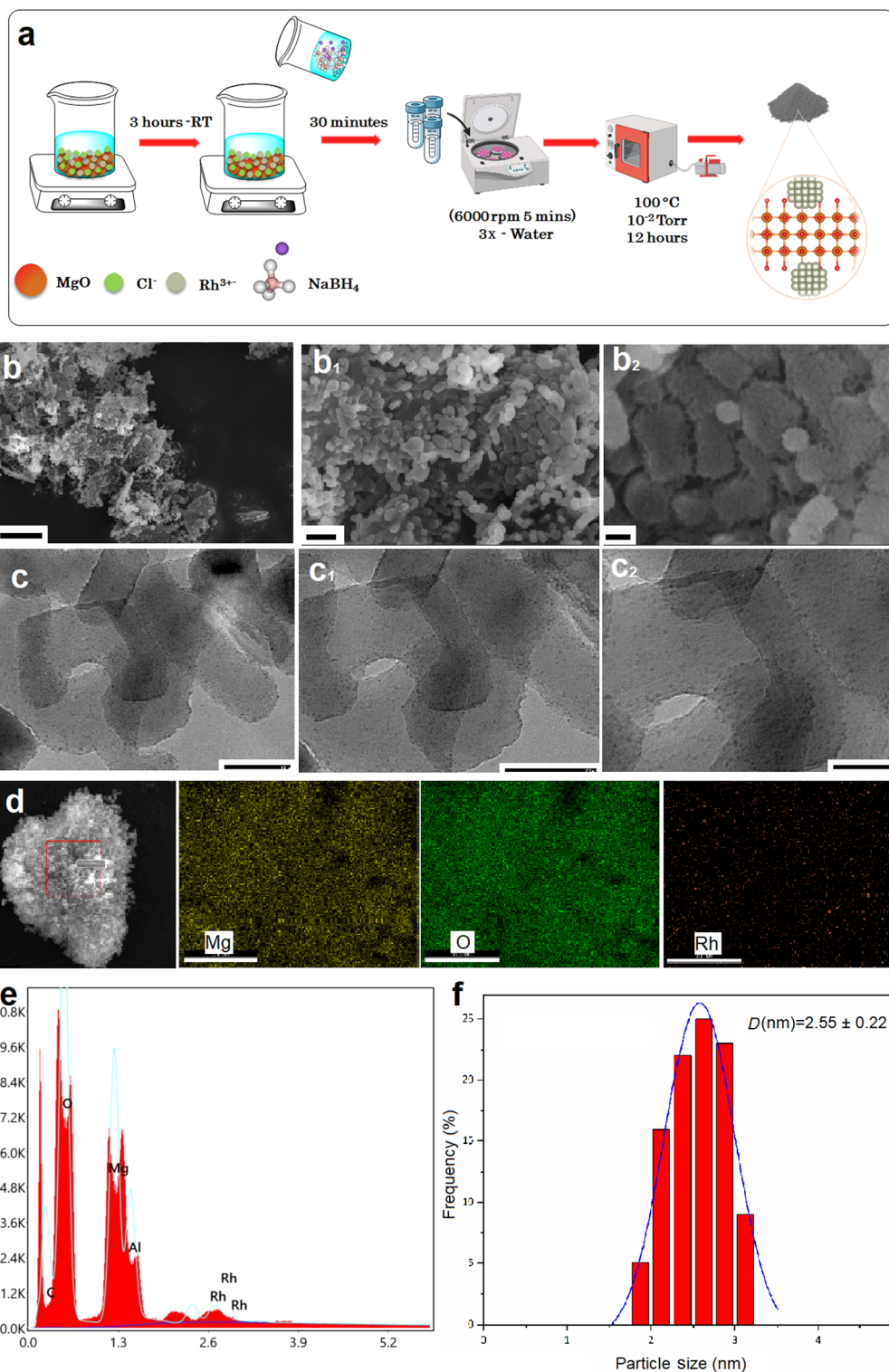This journal is © the Partner Organisations 2025

Fig. 1 (a) Schematic illustration of the preparation of the Rh@MgO catalyst. (b) SEM images of the Rh@MgO catalyst with scale bars from left to right: 1 μm, 200 nm, and 40 nm. (c) TEM images with scale bars from left to right: 200, 100, and 50 nm. (d) SEM image with corresponding EDX elemental mapping (scale bar: 500 nm) and (e) EDX spectrum. (f) TEM image-derived particle size distribution of the Rh nanoparticles.

ponding to Rh $(3d_{5/2})$ and Rh $(3d_{3/2})$, respectively. These peaks are characteristic of Rh in its metallic state $(Rh^0)$, indicating that the Rh nanoparticles remain in a reduced state on the MgO surface. However, the peak observed at 308.5 eV can be attributed to $Rh^{3+}$ $3d_{5/2}$, indicating the presence of $Rh_2O_3$, which likely results from the surface oxidation of Rh(0) nano-

This journal is © the Partner Organisations 2025

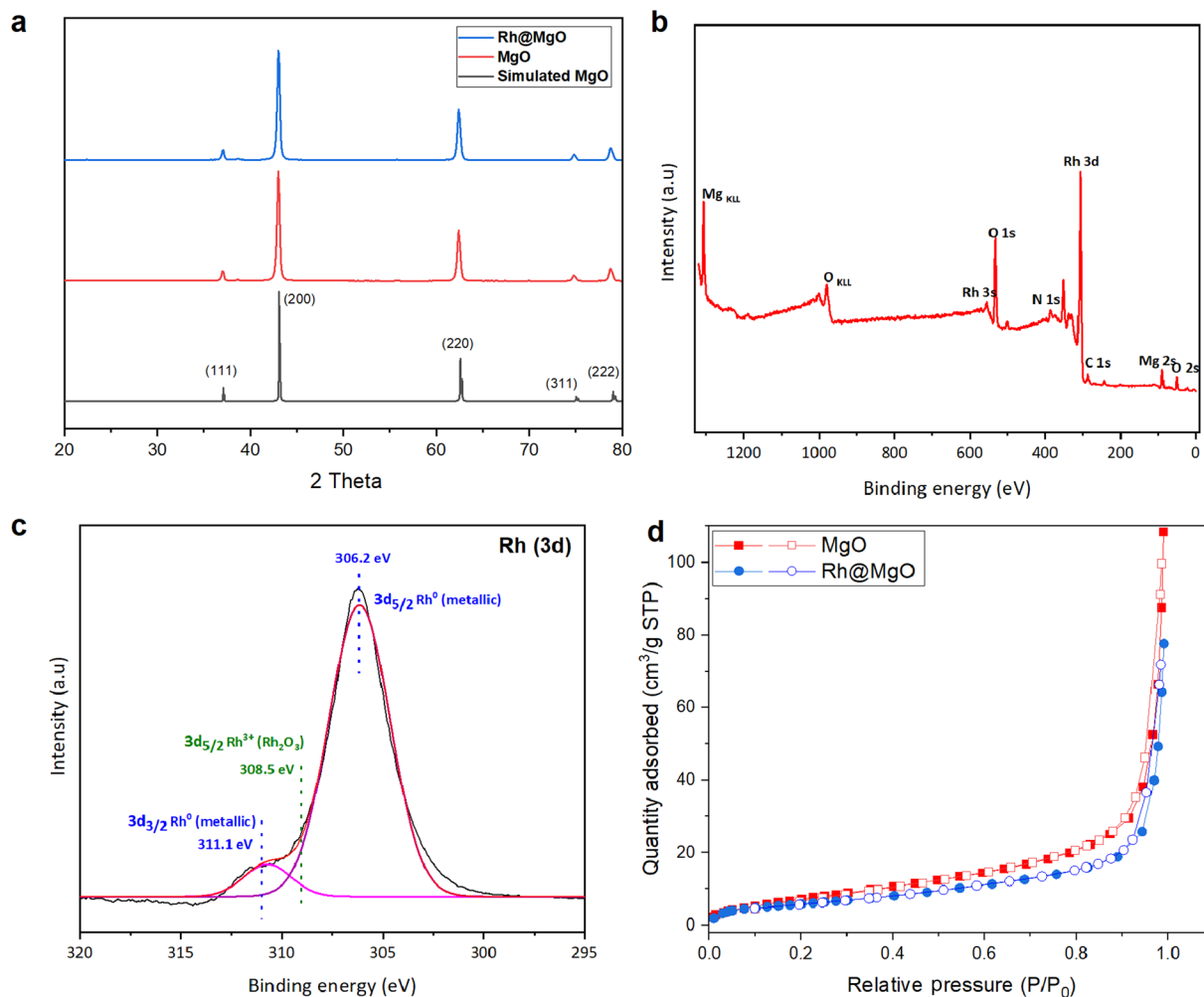*Inorg. Chem. Front.*, 2025, **12**, 342–354 | **345**

**Fig. 2** (a) Experimental PXRD patterns of MgO and Rh@MgO and a simulated PXRD pattern of MgO. (b) XPS survey of Rh@MgO. (c) Rh (3d) XPS spectra of Rh@MgO. (d) Nitrogen adsorption isotherms of MgO and Rh@MgO.

particles during the XPS sampling procedure.[49–51] Furthermore, in the Rh@MgO catalyst, the Rh (3d) peaks exhibit a shift to lower binding energies (from 311.85 and 307.14 eV in metallic Rh to 311.1 and 306.2 eV),[52,53] suggesting an increase in electron density on Rh due to electron transfer. This shift provides evidence for charge transfer at the Rh–MgO interface, enhancing the catalytic performance through electron enrichment of the Rh active sites. BET surface area measurements, obtained from $N_2$ isotherms at 77 K, show that MgO has a specific surface area of 76 $m^2$ $g^{-1}$, while Rh@MgO has a slightly lower specific surface area of 73 $m^2$ $g^{-1}$ (Fig. 2d). This decrease in surface area upon Rh loading suggests a partial blockage of the MgO surface by Rh, although the overall surface area remains relatively large, indicating minimal impact on the porosity of the support.

Computational studies on Rh@MgO systems[54–56] align with our experimental findings, demonstrating that Rh preferentially binds to oxygen sites on MgO (001) with significant adhesion energy, particularly at low coverages, resulting in stable dispersion. This is supported by SEM and TEM results,

which show well-dispersed Rh nanoparticles. Additionally, XPS analysis reveals Rh predominantly in its metallic state ($Rh^0$) with minor surface oxidation, consistent with computational results indicating that Rh retains its metallic character on MgO with only slight oxidation tendencies. This stable and well-dispersed Rh distribution is key to the effective performance of the catalyst.

### 3.2 Catalyst performance

Before conducting catalytic performance assessments, preliminary experiments were carried out to optimize sodium hydroxide (NaOH) concentration, as it plays a crucial role in promoting hydrazine borane (HB) decomposition. The addition of $OH^-$ promotes the reduction of undesirable $N_2H_5^+$ ($N_2H_5^+$ + $OH^- \rightarrow N_2H_4 + H_2O$), further facilitating hydrazine decomposition. The alkaline environment thus aids in breaking N–H and N–N bonds, promoting the formation of $N_2$ and $H_2$ while suppressing the generation of ammonia ($NH_3$).[57] According to the results (Fig. 3a), the Rh@MgO catalyst alone was unable to dehydrogenate the $N_2H_4$ component without NaOH, only cata-
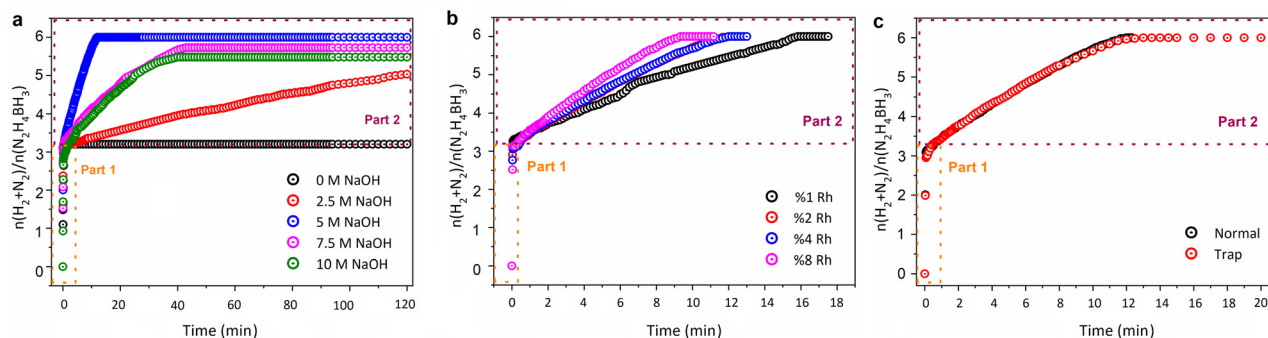
**346** | *Inorg. Chem. Front.*, 2025, **12**, 342–354

This journal is © the Partner Organisations 2025

**Fig. 3** Mole ratio of generated gas ($H_2 + N_2$)/HB *versus* time graph for the Rh@MgO-catalyzed dehydrogenation of aqueous HB depending on (a) NaOH concentration and (b) Rh content. (c) HCl trap control experiment. (For all, [HB] = 100 mM, $V_{Water}$ = 10 mL, Rh@MgO = 100 mg, reaction temp. = 50 °C.)

lyzing the hydrolysis of the –$BH_3$ group. Increasing NaOH concentration initially enhanced both the rate and conversion of the catalytic reaction, with optimum performance observed at 5.0 M. Beyond this concentration, catalytic activity decreased, likely due to the poisoning of active Rh centers by hydroxyl ions, which interact electrostatically with the metal surface (Fig. 3a).[58] Based on these findings, an NaOH concentration of 5.0 M was selected for further catalytic experiments.

Following the identification of the optimal base concentration, we proceeded to evaluate the effectiveness of different rhodium (Rh) molar ratios in Rh nanoclusters for the complete decomposition of hydrazine borane. Various molar ratios of Rh in the Rh@MgO catalyst were tested under consistent conditions to assess catalytic efficiency and conversion rates. Analysis of the data presented in Fig. 3b revealed: (i) the 1% Rh molar ratio catalyst exhibited markedly lower efficiency compared to higher Rh ratios, and (ii) the Rh@MgO catalysts with 2% and 4% Rh loadings showed comparable efficiencies (Fig. 3b). However, due to the high cost of the precious metal rhodium and considerations of atom economy, further experiments were conducted with the catalyst containing 2 wt% Rh. Additionally, in order to determine the role of the MgO support in the performance of the catalyst, catalytic tests were conducted on both MgO alone and a physical Rh/MgO mixture. The results show that while MgO alone exhibits no activity and the Rh/MgO mixture has limited efficiency due to Rh nanoparticle agglomeration, the Rh@MgO catalyst effectively prevents agglomeration, resulting in significantly enhanced catalytic performance for the dehydrogenation of hydrazine borane (Fig. S2†).

The composition of the gas produced during the Rh@MgO-catalyzed dehydrogenation of hydrazine borane was analyzed using mass spectrometry, confirming that it consisted exclusively of hydrogen ($H_2$) and nitrogen ($N_2$) in a molar ratio of 5.0/1.0. Consistent gas volumes were observed both in the absence and presence of an HCl trap, indicating no ammonia ($NH_3$) was produced during the reaction (Fig. 3c). This confirms that the Rh@MgO catalyst facilitates the generation of ammonia-free hydrogen from hydrazine borane in an aqueous alkaline environment. The Rh@MgO catalyst, containing

2 wt% Rh, exhibits exceptional performance, achieving complete conversion (100%) and a high turnover frequency (2005.34 h$^{-1}$), surpassing many catalysts reported in the literature[15,16,26,59–61] (also see Table S1†). Additionally, its composition, featuring a relatively inexpensive and readily available single-metal support, offers a significant advantage over the more complexly designed catalysts commonly found in academic and industrial research.

Upon establishing the optimal base concentration, detailed kinetics studies were conducted to ascertain the effects of both catalyst and substrate (hydrazine borane, HB) quantities on the catalytic reaction rate. These studies dissected the complete degradation reaction of hydrazine borane into two primary stages: the initial hydrolysis of the $BH_3$ moiety followed by the subsequent decomposition of the $N_2H_4$ moiety, each analyzed separately in the kinetics experiments.[61] The results depicted in Fig. 4a illustrate the outcomes of these experiments, where the complete decomposition reaction of an equivalent amount of hydrazine borane (100 mM, 23 mg) was examined at a constant temperature (50 °C) using the Rh@MgO catalyst at varying molar ratios of active metals. The plot shows the ratio of released gases ($H_2 + N_2$) to the molar concentration of hydrazine borane *versus* time. As anticipated, an increase in catalyst concentration led to an increased rate of the catalytic reaction. This increment is further explored through the graph of the logarithmic values of the initial rate constants ($k_{obs}$) *versus* the catalyst concentration, as shown in Fig. 4b. The analysis yielded slopes of 0.41 for part 1 (hydrolysis of $BH_3$) and 1.94 for part 2 (decomposition of $N_2H_4$), indicating that part 1 is first order and part 2 is second order in relation to the Rh concentration within the catalytic complete degradation reaction of hydrazine borane.

Further investigations explored the impact of hydrazine borane (HB) concentration on the catalytic reaction rate, with kinetics studies conducted by varying the initial HB amounts while keeping the catalyst concentration (1.5 mM) and temperature (50 °C) constant. As shown in Fig. 4c, the complete catalytic decomposition of HB at different starting substrate concentrations reveals distinct behaviors in two phases of the reaction. The plot of gas released ($H_2 + N_2$) relative to the
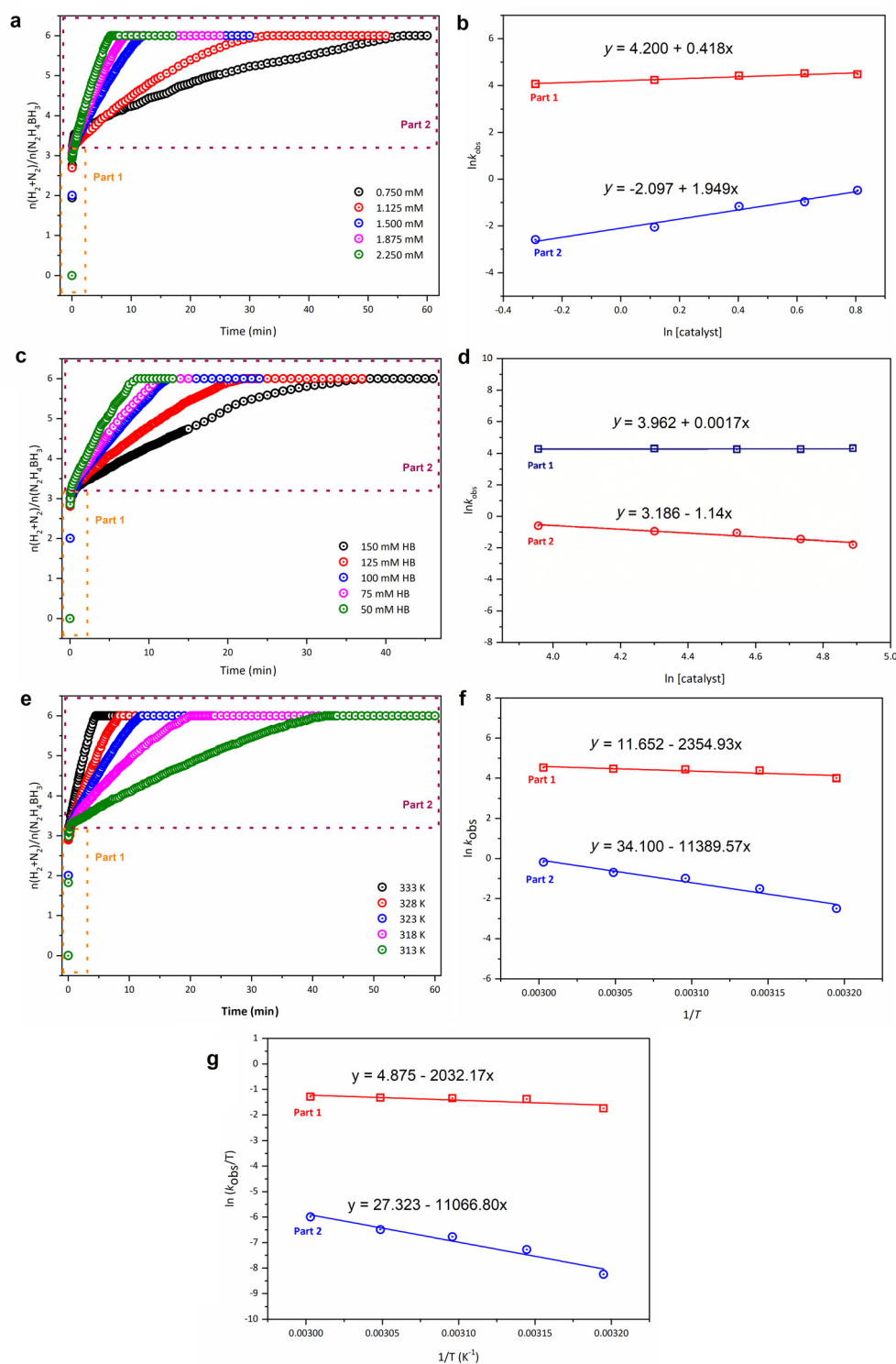
This journal is © the Partner Organisations 2025

*Inorg. Chem. Front.*, 2025, **12**, 342–354 | **347**

**Fig. 4** Mole ratio of generated gas ($H_2 + N_2$)/HB *versus* time graph for the Rh@MgO-catalyzed dehydrogenation of aqueous HB depending on (a) catalyst concentrations, (c) substrate concentration and (e) temperature. Logarithmic plots of the observed rate constants ($k_{obs}$) *versus* (b) catalyst and (d) substrate concentrations. (f) Arrhenius plot and (g) Eyring plot.

molar concentration of HB over time shows that the reaction rate in part 1 remains approximately constant across all substrate concentrations, indicating zero-order kinetics with respect to HB. In contrast, part 2 demonstrates a noticeable decline in the reaction rate as substrate concentration increases, suggesting a negative-order kinetics behavior, likely

due to substrate inhibition or saturation effects. The slopes obtained from the logarithmic plots of rate constants ($k_{obs}$) versus substrate concentration, as shown in Fig. 4d, were 0.0017 for part 1 and −1.14 for part 2, further confirming the distinct kinetics mechanisms governing each phase of the reaction.

To further investigate the dependency of the Rh@MgO-catalyzed complete degradation reaction of hydrazine borane (HB) on both catalyst and substrate concentrations at varying temperatures, and to calculate activation parameters such as activation energy ($E_a$), activation enthalpy ($\Delta H^{\#}$), and activation entropy ($\Delta S^{\#}$), experiments were conducted with constant concentrations of Rh@MgO and HB at different temperatures. The results, shown in Fig. 4e, reveal that the reaction rates for both parts of the catalytic process increase with rising temperature, consistent with typical kinetics behavior. The calculated rate constants were used to construct Arrhenius and Eyring plots, as shown in Fig. 4f and g. These plots yielded activation energies of 19.6 kJ mol$^{-1}$ for part 1 and 94.7 kJ mol$^{-1}$ for part 2, with the lower activation energy of part 1 indicating a faster and more energy-efficient process than the slower, higher-energy part 2.

From the Eyring–Polanyi analysis, the activation parameters were derived, showing activation enthalpy ($\Delta H^{\#}$) values of $\Delta H^{\#1}$ = 16.89 kJ mol$^{-1}$ for part 1 and $\Delta H^{\#2}$ = 92 kJ mol$^{-1}$ for part 2. The corresponding activation entropy ($\Delta S^{\#}$) values were $\Delta S^{\#1}$ = −157.05 J mol$^{-1}$ K$^{-1}$ for part 1 and $\Delta S^{\#2}$ = 29.59 J mol$^{-1}$ K$^{-1}$ for part 2. The negative entropy value for part 1 suggests an associative mechanism, where the transition state is more ordered, likely involving the hydrolysis of BH$_3$. In contrast, the positive entropy value for part 2 indicates a dissociative mechanism, possibly involving the decomposition of N$_2$H$_4$, where the transition state is more disordered.

Additionally, turnover frequencies (CF) calculated at different temperatures (313, 318, 323, 328, and 333 K) provide further insights into the reaction dynamics. Part 1, which involves the hydrolysis of BH$_3$, exhibits significantly higher turnover frequencies, confirming its faster catalytic activity. Part 2, which is associated with the decomposition of N$_2$H$_4$, shows lower turnover frequencies, with the basic nature of the

environment playing a critical role in affecting the overall reaction rate. In summary, the kinetics and thermodynamics data indicate that part 1 proceeds *via* an energy-efficient, associative mechanism with low activation energy, while part 2 follows a dissociative mechanism with significantly higher energy requirements, reflecting the complexity of nitrogen release.

The catalytic stability of the Rh@MgO catalyst was rigorously evaluated through a series of recyclability experiments. These experiments, documented in Fig. 5, showed that when all HB was converted into N$_2$ and H$_2$ in a given cycle, an equivalent amount of fresh HB was added to the system, and the reaction was continued for up to five consecutive cycles. Despite a reduction in the catalyst activity due to partial deactivation—such as potential surface poisoning, structural changes, or minor agglomeration of the Rh nanoparticles—Rh@MgO continues to achieve full hydrogen yield in the dehydrogenation of HB, maintaining 100% selectivity (Fig. 5a). Post-recycling, TEM, XPS and ICP-OES analyses of the recovered Rh@MgO catalyst and reaction solution confirmed minimal leaching and agglomeration (Fig. 5b and c, Fig. S3†), underlining the robustness and stability of the Rh@MgO catalyst in the complete degradation reaction of hydrazine borane over multiple cycles.

To further elucidate the superior catalytic activity of the Rh@MgO catalyst, a comprehensive set of comparative studies was conducted. Initially, monometallic clusters consisting of Pt, Ir, Mo, and Ni, along with 2% by mass Rh, were synthesized on MgO supports. Under identical reaction conditions, Rh@MgO demonstrated enhanced performance in the complete decomposition of hydrazine borane (HB) compared to other monometal@MgO catalysts (Fig. 6a). Subsequently, to assess the impact of the solid support material, Rh@MgO catalysts were developed using alternative supports including TiO$_2$, CeO$_2$, ZrO$_2$, Al$_2$O$_3$, SiO$_2$, and HTaL (hydrotalcite) at comparable ratios and subjected to the same reaction conditions for the degradation of HB. The outcomes revealed that Rh@MgO exhibited the highest catalytic activity among these configurations (Fig. 6b), with TEM imaging confirming that Rh@MgO featured the smallest Rh particle size and the most uniform distribution (Fig. S1†). In the final phase of the study, to evalu-
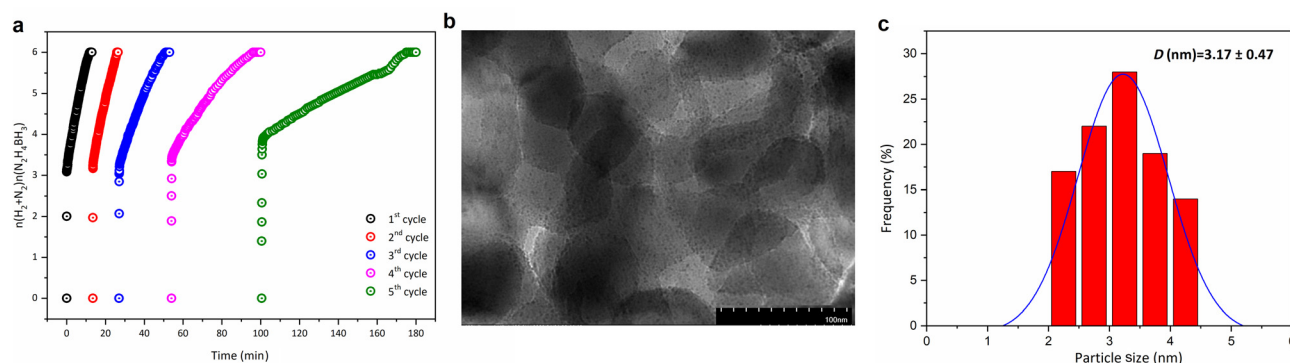


**Fig. 5** (a) Comparison of the catalytic performance of the Rh@MgO catalyst for five consecutive catalytic cycles. (b) TEM image of the catalyst after the 5th cycle and (c) particle size distributions obtained from this image.
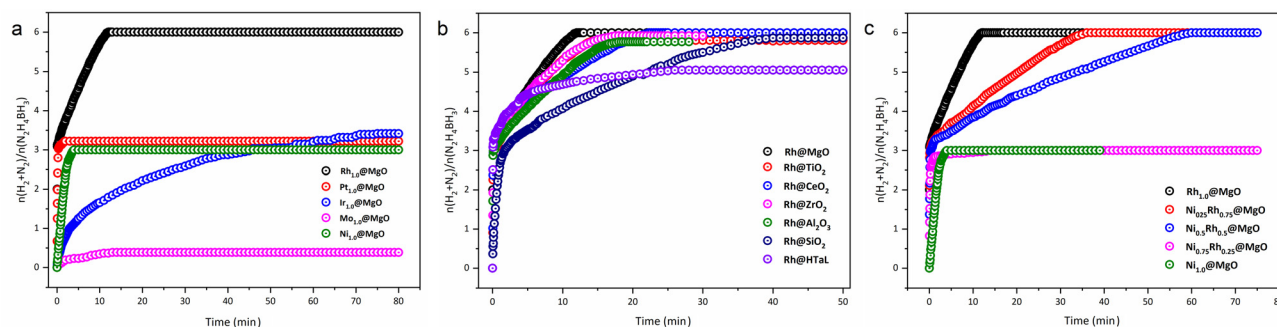
**Fig. 6** Comparison of the catalytic performance of the Rh@MgO catalyst in the complete dehydrogenation of HB under the same conditions with different catalysts: (a) TM@MgO (TM = transition metal), (b) Rh@MO (MO = metal oxide), and (c) Rh$_x$Ni@MgO. (For all, [HB] = 100 mM, V$_{Water}$ = 10 mL, [NaOH] = 5 M, reaction temp. = 50 °C.)

ate cost-effectiveness, Ni$_x$Rh(1 − x) (x = 0.0, 0.25, 0.5, 0.75, and 1.0) bimetallic catalyst clusters were synthesized on MgO supports, integrating nickel known for its catalytic prowess. The results indicated that the monometallic Ni$_{1.0}$@MgO and the bimetallic Ni$_{0.75}$Rh$_{0.25}$@MgO catalysts primarily facilitated the hydrolysis of the BH$_3$ moiety (part 1) but did not exhibit complete catalytic activity. Conversely, Rh$_{1.0}$@MgO, along with bimetallic Ni$_{0.25}$Rh$_{0.75}$@MgO catalysts, achieved a 100% yield in catalytic activity. However, the activity rate of Rh$_{1.0}$@MgO was significantly superior to those of the bimetallic variants (Fig. 6c).

The remarkable catalytic performance of Rh@MgO in the dehydrogenation of hydrazine borane (HB) can be attributed to the synergistic interaction between Rh and the MgO support. On the MgO surface, oxygen anions (O$^{2-}$) are rich in electron density, making them highly reactive towards electron-deficient Rh atoms. These O$^{2-}$ ions serve as electron donors, interacting with the d-orbitals of Rh, allowing the Rh atoms, particularly at low coverages, to preferentially bind to the oxygen sites on the MgO surface. This binding is driven by a combination of charge transfer and polarization effects, with charge transfer playing a dominant role in stabilizing the Rh atoms. Additionally, the low surface energy of MgO provides a stable platform for Rh adsorption without inducing significant structural changes to the surface, ensuring a uniform and well-dispersed distribution of Rh nanoparticles.[54,62–64] This uniform dispersion enhances the performance of the catalyst by preventing Rh agglomeration and maximizing the available
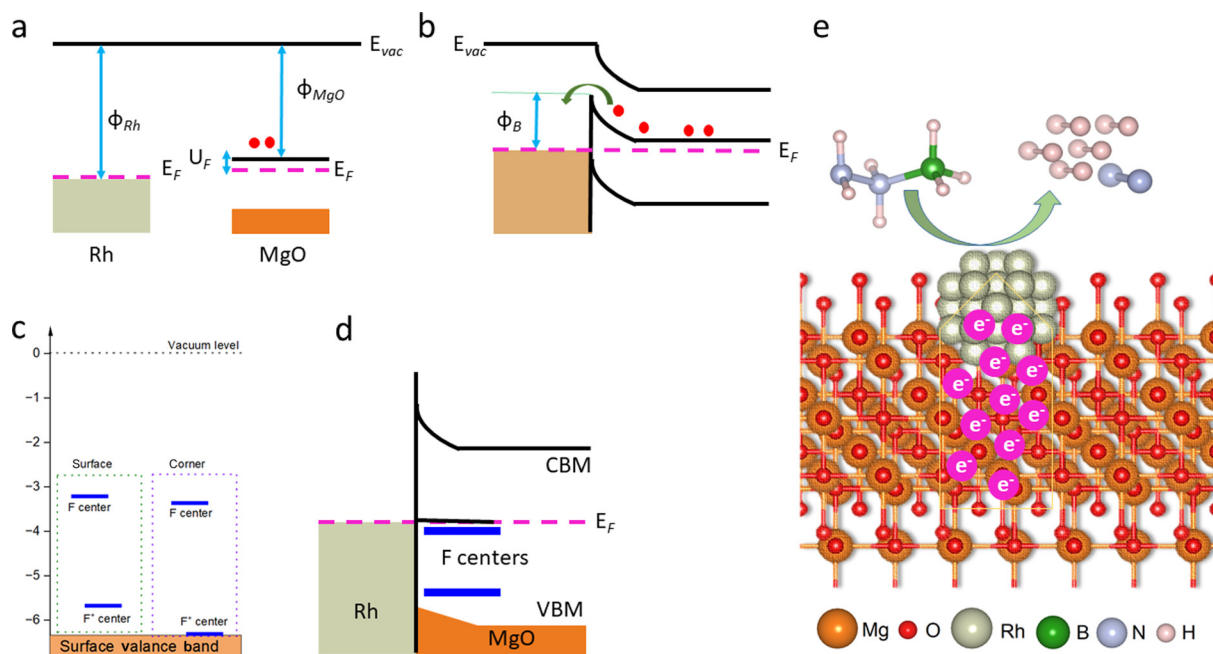


**Fig. 7** Energy band diagram of Rh and MgO: (a) before and (b) after contact. (c) Illustration depicting the energy levels of various states of MgO. (d) Illustration of the Fermi level-pinned state at the Rh@MgO interface. (e) Schematic diagram of the proposed mechanism for Rh@MgO-catalyzed dehydrogenation of hydrazine borane (HB).

**350** | *Inorg. Chem. Front.*, 2025, **12**, 342–354

This journal is © the Partner Organisations 2025

surface area for catalytic reactions. Furthermore, the stability of the MgO surface contributes to the strength of the Rh–O bond, as MgO is resistant to significant surface reconstruction or new defect formation. As a result, Rh atoms interact with a well-defined, stable surface, which facilitates uniform binding and promotes high catalytic activity.

From a mechanistic perspective, in reactions where electron donation is required, such as dehydrogenation, it is important that the work function, defined as the energy difference between the Fermi level ($E_F$) and the vacuum level, is low. When a transition metal and a support come into contact, as in the Rh@MgO catalyst, a Schottky barrier forms at the metal/metal oxide interface, with its height determined by the difference in their work functions ($\phi^{TM} - \phi^{support}$) (Fig. 7a). This barrier acts as a potential energy barrier for charge carriers, particularly electrons, and plays a crucial role in determining electron movement across the interface. A lower Schottky barrier enables smoother electron flow, which can enhance reaction rates by allowing electrons to move more freely between the metal and the substrate (Fig. 7b). Conversely, a higher barrier impedes electron movement, reducing catalytic efficiency.[65,66] In the case of Rh@MgO, the reported work functions are close: approximately 5.2 eV for Rh[67] and 5.0 eV for MgO.[68] This minimal difference suggests a low Schottky barrier at the Rh@MgO interface, likely promoting efficient electron transfer from MgO to Rh, contributing to enhanced catalytic performance. Additionally, experimental evidence suggests that metal nucleation typically occurs preferentially at defects rather than on the well-ordered terraces of oxide surfaces, with oxygen vacancies or color centers (F-centers) playing a crucial role[62,69] (Fig. 7c). During the growth of Rh clusters on the MgO surface, Rh atoms interact with the terraces of the oxide support.[70] Electrons localize in these vacancies, and the energy levels of these electrons align with the Fermi level of Rh, a phenomenon known as Fermi level pinning (FLP)[68] (Fig. 7d). This results in a significant reduction in the work function of MgO. Thus, there could be an intensive electron transfer from MgO to Rh, which promotes the decomposition of $N_2H_4$ by breaking N–H bonds, making Rh more reactive towards hydrazine borane (HB)[57] (Fig. 7e).

## 4. Conclusion

In summary, we successfully immobilized monodisperse Rh nanoparticles on an MgO solid support, resulting in the Rh@MgO catalyst, which exhibited exceptional catalytic performance in the dehydrogenation of hydrazine borane (HB). The catalyst, containing only 2 wt% Rh, achieved a remarkable turnover frequency (TOF) of 2005.34 h$^{-1}$ at 50 °C with 100% H$_2$ selectivity. Comparative studies revealed that Rh@MgO outperformed various other structures, including Rh on different metal oxide nanoparticles, other transition metal catalysts on MgO, and Ni grown on MgO in both single-phase and bimetallic (Rh/Ni) forms. The extraordinary performance of

Rh@MgO can be attributed to the synergistic interaction between Rh and MgO, characterized by several key factors. The homogeneous dispersion of ultrafine, monodisperse Rh particles on the MgO support significantly enhanced catalytic activity. Additionally, the close proximity of the work functions of Rh and MgO contributed to a low-energy Schottky barrier, facilitating efficient electron transfer from MgO to Rh. Furthermore, electrons localized in surface defects (at F-centers) during the attachment of the Rh nanoparticles may have aligned with the Fermi level of Rh through the phenomenon of Fermi level pinning (FLP), further improving electron transfer. This made the MgO support an effective electron donor to the Rh catalytic sites, leading to enhanced catalytic efficiency in HB dehydrogenation under mild conditions. The combination of low Rh content and cost-effective MgO support presents a promising pathway not only for laboratory-scale research but also for practical industrial applications. Our findings demonstrate the potential of the Rh@MgO catalyst as a highly efficient and economically viable option for future catalytic processes.

## Data availability

The data supporting this article have been included as part of the ESI.†

## Conflicts of interest

There are no conflicts to declare.

## Acknowledgements

## References

1 C. McGlade and P. Ekins, The geographical distribution of fossil fuels unused when limiting global warming to 2 °C, *Nature*, 2015, **517**(7533), 187–190, DOI: **10.1038/nature14016**–U143.

2 M. Höök and X. Tang, Depletion of fossil fuels and anthropogenic climate change-A review, *Energy Policy*, 2013, **52**, 797–809, DOI: **10.1016/j.enpol.2012.10.046**.

3 W. J. Fang, C. L. Ding, L. Chen, W. Q. Zhou, J. F. Wang, K. Huang, R. Zhu, J. Wu, B. F. Liu, Q. Fang, *et al.*, Review of Hydrogen Storage Technologies and the Crucial Role of Environmentally Friendly Carriers, *Energy Fuel*, 2024, **38**(15), 13539–13564, DOI: **10.1021/acs.energyfuels.4c01781**.

This journal is © the Partner Organisations 2025

*Inorg. Chem. Front.*, 2025, **12**, 342–354 | **351**

4 M. P. Suh, H. J. Park, T. K. Prasad and D.-W. Lim, Hydrogen Storage in Metal–Organic Frameworks, *Chem. Rev.*, 2012, **112**(2), 782–835, DOI: **10.1021/cr200274s**.

5 Y. Wang, Y. Xue and A. Züttel, Nanoscale engineering of solid-state materials for boosting hydrogen storage, *Chem. Soc. Rev.*, 2024, **53**(2), 972–1003, DOI: **10.1039/D3CS00706E**.

6 M. Erkartal and U. Sen, Boronic Acid Moiety as Functional Defect in UiO-66 and Its Effect on Hydrogen Uptake Capacity and Selective COAdsorption: A Comparative Study, *ACS Appl. Mater. Interfaces*, 2018, **10**(1), 787–795, DOI: **10.1021/acsami.7b16937**.

7 L. Yan, J. Liang, D. Song, X. Li and H. Li, Modulation of Charge Redistribution in Heterogeneous NiO-Ni3Se4 Nanosheet Arrays for Advanced Water Electrolysis, *Adv. Funct. Mater.*, 2024, **34**(4), 2308345, DOI: **10.1002/adfm.202308345**.

8 Y. Huang, Y. Cheng and J. Zhang, A Review of High Density Solid Hydrogen Storage Materials by Pyrolysis for Promising Mobile Applications, *Ind. Eng. Chem. Res.*, 2021, **60**(7), 2737–2771, DOI: **10.1021/acs.iecr.0c04387**.

9 A. Schneemann, J. L. White, S. Kang, S. Jeong, L. F. Wan, E. S. Cho, T. W. Heo, D. Prendergast, J. J. Urban, B. C. Wood, *et al.*, Nanostructured Metal Hydrides for Hydrogen Storage, *Chem. Rev.*, 2018, **118**(22), 10775–10839, DOI: **10.1021/acs.chemrev.8b00313**.

10 Y. Li, J. Liao, Y. Feng, J. Li, Q. Liu, W. Zhou, M. He and H. Li, Built-in Electric Field in Yolk Shell CuO-Co3O4@Co3O4 with Modulated Interfacial Charge to Facilitate Hydrogen Production from Ammonia Borane Methanolysis Under Visible Light, *Adv. Funct. Mater.*, 2024, **34**(46), 2405361, DOI: **10.1002/adfm.202405361**, (acccessed 2024/11/13).

11 J. Liao, Y. Shao, Y. Feng, J. Zhang, C. Song, W. Zeng, J. Tang, H. Dong, Q. Liu and H. Li, Interfacial charge transfer induced dual-active-sites of heterostructured Cu0.8Ni0.2WO4 nanoparticles in ammonia borane methanolysis for fast hydrogen production, *Appl. Catal., B*, 2023, **320**, 121973, DOI: **10.1016/j.apcatb.2022.121973**.

12 H.-Z. Wang, Y.-X. Shao, Y.-F. Feng, Y.-J. Tan, Q.-Y. Liao, X.-D. Chen, X.-F. Zhang, Z.-H. Guo and H. Li, Heterostructured Co3O4−SnO2 composites containing oxygen vacancy with high activity and recyclability toward NH3BH3 dehydrogenation, *Rare Met.*, 2023, **42**(9), 3013–3023, DOI: **10.1007/s12598-023-02305-0**.

13 J. Liao, Y. Wu, Y. Shao, Y. Feng, X. Zhang, W. Zhang, J. Li, M. Wu, H. Dong, Q. Liu and H. Li, Ammonia borane methanolysis for hydrogen evolution on Cu3Mo2O9/NiMoO4 hollow microspheres, *Chem. Eng. J.*, 2022, **449**, 137755, DOI: **10.1016/j.cej.2022.137755**.

14 T. Hügle, M. F. Kühnel and D. Lentz, Hydrazine Borane: A Promising Hydrogen Storage Material, *J. Am. Chem. Soc.*, 2009, **131**(21), 7444–7446, DOI: **10.1021/ja9013437**.

15 Z. Zhang, S. Zhang, Q. Yao, X. Chen and Z.-H. Lu, Controlled Synthesis of MOF-Encapsulated NiPt Nanoparticles toward Efficient and Complete Hydrogen Evolution from Hydrazine Borane and Hydrazine, *Inorg. Chem.*, 2017, **56**(19), 11938–11945, DOI: **10.1021/acs.inorgchem.7b01910**.

16 X. Zhang, Q. Yao, Y. Wang, M. Liu and Z.-H. Lu, Hydrogen production from complete dehydrogenation of hydrazine borane on carbon-doped TiO2-supported NiCr catalysts, *Inorg. Chem. Front.*, 2024, **11**(6), 1683–1692, DOI: **10.1039/D3QI02633G**.

17 J. J. Long, Q. L. Yao, X. L. Zhang, H. C. Wu and Z. H. Lu, Defects engineering of metal-organic framework immobilized Ni-La(OH)3 nanoparticles for enhanced hydrogen production, *Appl. Catal., B*, 2023, **320**, 121989, DOI: **10.1016/j.apcatb.2022.121989**.

18 Q. Yao, Z.-H. Lu, R. Zhang, S. Zhang, X. Chen and H.-L. Jiang, A noble-metal-free nanocatalyst for highly efficient and complete hydrogen evolution from N2H4BH3, *J. Mater. Chem. A*, 2018, **6**(10), 4386–4393, DOI: **10.1039/C7TA10886A**.

19 H. Zou, F. Guo, M. Luo, Q. Yao and Z.-H. Lu, La(OH)3-decorated NiFe nanoparticles as efficient catalyst for hydrogen evolution from hydrous hydrazine and hydrazine borane, *Int. J. Hydrogen Energy*, 2020, **45**(20), 11641–11650, DOI: **10.1016/j.ijhydene.2020.02.074**.

20 Q.-L. Zhu, D.-C. Zhong, U. B. Demirci and Q. Xu, Controlled Synthesis of Ultrafine Surfactant-Free NiPt Nanocatalysts toward Efficient and Complete Hydrogen Generation from Hydrazine Borane at Room Temperature, *ACS Catal.*, 2014, **4**(12), 4261–4268, DOI: **10.1021/cs501329c**.

21 D. Çelik, S. Karahan, M. Zahmakıran and S. Özkar, Hydrogen generation from the hydrolysis of hydrazine-borane catalyzed by rhodium(0) nanoparticles supported on hydroxyapatite, *Int. J. Hydrogen Energy*, 2012, **37**(6), 5143–5151, DOI: **10.1016/j.ijhydene.2011.12.067**.

22 S. Karahan, M. Zahmakıran and S. Özkar, Catalytic methanolysis of hydrazine borane: a new and efficient hydrogen generation system under mild conditions, *Dalton Trans.*, 2012, **41**(16), 4912–4918, DOI: **10.1039/C2DT11867J**.

23 Z. Zhang, Z.-H. Lu and X. Chen, Ultrafine Ni–Pt Alloy Nanoparticles Grown on Graphene as Highly Efficient Catalyst for Complete Hydrogen Generation from Hydrazine Borane, *ACS Sustainable Chem. Eng.*, 2015, **3**(6), 1255–1261, DOI: **10.1021/acssuschemeng.5b00250**.

24 J. Hannauer, O. Akdim, U. B. Demirci, C. Geantet, J.-M. Herrmann, P. Miele and Q. Xu, High-extent dehydrogenation of hydrazine borane N2H4BH3 by hydrolysis of BH3 and decomposition of N2H4, *Energy Environ. Sci.*, 2011, **4**(9), 3355–3358, DOI: **10.1039/C1EE01886H**.

25 J. Wang, B. Hui, T. Jia, X. Chen, X. Yu, L. Li, X. Zhang, Z. Lu and X. Yang, PVP-Adjusted Crystal Surfaces of PtPd Nanoparticles for Enhancing the Catalytic Hydrolysis of Ammonia Borane, *ACS Appl. Nano Mater.*, 2024, **7**(8), 9490–9498, DOI: **10.1021/acsanm.4c00947**.

26 Q. Yao, M. He, X. Hong, X. Chen, G. Feng and Z.-H. Lu, Hydrogen production via selective dehydrogenation of hydrazine borane and hydrous hydrazine over MoOx-pro-

**352** | *Inorg. Chem. Front.*, 2025, **12**, 342–354

This journal is © the Partner Organisations 2025

moted Rh catalyst, *Int. J. Hydrogen Energy*, 2019, **44**(53), 28430–28440, DOI: **10.1016/j.ijhydene.2019.02.105**.

27  D.-C. Zhong, K. Aranishi, A. K. Singh, U. B. Demirci and Q. Xu, The synergistic effect of Rh–Ni catalysts on the highly-efficient dehydrogenation of aqueous hydrazine borane for chemical hydrogen storage, *Chem. Commun.*, 2012, **48**(98), 11945–11947, DOI: **10.1039/C2CC36407G**.

28  M. Rakap, Catalytic hydrolysis of hydrazine borane to release hydrogen by cobalt-ruthenium nanoclusters, *Int. J. Hydrogen Energy*, 2020, **45**(31), 15611–15617, DOI: **10.1016/j.ijhydene.2020.04.042**.

29  Q. Yao, Z.-H. Lu, K. Yang, X. Chen and M. Zhu, Ruthenium nanoparticles confined in SBA-15 as highly efficient catalyst for hydrolytic dehydrogenation of ammonia borane and hydrazine borane, *Sci. Rep.*, 2015, **5**(1), 15186, DOI: **10.1038/srep15186**.

30  S. Karahan, M. Zahmakıran and S. Özkar, Catalytic hydrolysis of hydrazine borane for chemical hydrogen storage: Highly efficient and fast hydrogen generation system at room temperature, *Int. J. Hydrogen Energy*, 2011, **36**(8), 4958–4966, DOI: **10.1016/j.ijhydene.2010.12.129**.

31  X. Liang, N. Fu, S. Yao, Z. Li and Y. Li, The Progress and Outlook of Metal Single-Atom-Site Catalysis, *J. Am. Chem. Soc.*, 2022, **144**(40), 18155–18174, DOI: **10.1021/jacs.1c12642**.

32  L. Liu and A. Corma, Metal Catalysts for Heterogeneous Catalysis: From Single Atoms to Nanoclusters and Nanoparticles, *Chem. Rev.*, 2018, **118**(10), 4981–5079, DOI: **10.1021/acs.chemrev.7b00776**.

33  Z. Li, S. Ji, Y. Liu, X. Cao, S. Tian, Y. Chen, Z. Niu and Y. Li, Well-Defined Materials for Heterogeneous Catalysis: From Nanoparticles to Isolated Single-Atom Sites, *Chem. Rev.*, 2020, **120**(2), 623–682, DOI: **10.1021/acs.chemrev.9b00311**.

34  T. S. Rodrigues, A. G. M. da Silva and P. H. C. Camargo, Nanocatalysis by noble metal nanoparticles: controlled synthesis for the optimization and understanding of activities, *J. Mater. Chem. A*, 2019, **7**(11), 5857–5874, DOI: **10.1039/C9TA00074G**.

35  S. Ma, W. Han, W. Han, F. Dong and Z. Tang, Recent advances and future perspectives in MOF-derived single-atom catalysts and their application: a review, *J. Mater. Chem. A*, 2023, **11**(7), 3315–3363, DOI: **10.1039/D2TA08735A**.

36  H. Huang, K. Shen, F. Chen and Y. Li, Metal–Organic Frameworks as a Good Platform for the Fabrication of Single-Atom Catalysts, *ACS Catal.*, 2020, **10**(12), 6579–6586, DOI: **10.1021/acscatal.0c01459**.

37  Y.-S. Wei, M. Zhang, R. Zou and Q. Xu, Metal–Organic Framework-Based Catalysts with Single Metal Sites, *Chem. Rev.*, 2020, **120**(21), 12089–12174, DOI: **10.1021/acs.chemrev.9b00757**.

38  M. Liu, C. Miao and Z. Wu, Recent advances in the synthesis, characterization, and catalytic consequence of metal species confined within zeolite for hydrogen-related reactions, *Ind. Chem. Mater.*, 2024, **2**(1), 57–84, DOI: **10.1039/D3IM00074E**.

39  R. Lang, X. Du, Y. Huang, X. Jiang, Q. Zhang, Y. Guo, K. Liu, B. Qiao, A. Wang and T. Zhang, Single-Atom Catalysts Based on the Metal–Oxide Interaction, *Chem. Rev.*, 2020, **120**(21), 11986–12043, DOI: **10.1021/acs.chemrev.0c00797**.

40  K. Polychronopoulou, K. Giannakopoulos and A. M. Efstathiou, Tailoring MgO-based supported Rh catalysts for purification of gas streams from phenol, *Appl. Catal., B*, 2012, **111–112**, 360–375, DOI: **10.1016/j.apcatb.2011.10.019**.

41  X. Liu, W. Chen, J. Zou, L. Ye and Y. Yuan, Liquid-Phase Amination of Phenol to Aniline over the Pd/MgO Catalyst without External Hydrogen Addition, *ACS Sustainable Chem. Eng.*, 2022, **10**(21), 6988–6998, DOI: **10.1021/acssuschemeng.2c00273**.

42  Y.-j. Hao, L.-g. Tian, E. Duan, J. Liu, T.-y. Qi, W.-q. Kong, X.-h. Qi, X. Liu, Y. Liu, J. Zhao and F.-t. Li, Low-Temperature Methane Oxidation Triggered by Peroxide Radicals over Noble-Metal-Free MgO Catalyst, *ACS Appl. Mater. Interfaces*, 2020, **12**(19), 21761–21771, DOI: **10.1021/acsami.0c04083**.

43  A. S. Khder, H. M. Altass, R. S. Jassas, M. M. Al-Rooqi, M. A. Khder, M. Morad, A. Gebreil, Z. Moussa and S. A. Ahmed, Room-Temperature CO Oxidation over Au–Pd Monometallic and Bimetallic Nanoparticle-Supported MgO, *ACS Appl. Nano Mater.*, 2023, **6**(6), 4243–4252, DOI: **10.1021/acsanm.2c05326**.

44  L. Zhang, J. Han, Y. Wang, W. Yang and S. Tao, Pd/Mg(OH)2/MgO–ZrO2 Nanocomposite Systems for Highly Efficient Suzuki–Miyaura Coupling Reaction at Room Temperature: Implications for Low-Carbon Green Organic Synthesis, *ACS Appl. Nano Mater.*, 2022, **5**(6), 8059–8069, DOI: **10.1021/acsanm.2c01179**.

45  M. Celebi, M. Yurderi, A. Bulut, M. Kaya and M. Zahmakiran, Palladium nanoparticles supported on amine-functionalized SiO$_2$ for the catalytic hexavalent chromium reduction, *Appl. Catal., B*, 2016, **180**, 53–64, DOI: **10.1016/j.apcatb.2015.06.020**.

46  M. A. Khalily, M. Yurderi, A. Haider, A. Bulut, B. Patil, M. Zahmakiran and T. Uyar, Atomic Layer Deposition of Ruthenium Nanoparticles on Electrospun Carbon Nanofibers: A Highly Efficient Nanocatalyst for the Hydrolytic Dehydrogenation of Methylamine Borane, *ACS Appl. Mater. Interfaces*, 2018, **10**(31), 26162–26169, DOI: **10.1021/acsami.8b04822**.

47  X. Hong, Q. Yao, M. Huang, H. Du and Z.-H. Lu, Bimetallic NiIr nanoparticles supported on lanthanum oxy-carbonate as highly efficient catalysts for hydrogen evolution from hydrazine borane and hydrazine, *Inorg. Chem. Front.*, 2019, **6**(9), 2271–2278, DOI: **10.1039/C9QI00848A**.

48  I. Fongkaew, B. Yotburut, W. Sailuam, W. Jindata, T. Thiwatwaranikul, A. Khamkongkaeo, N. Chuewangkam, N. Tanapongpisit, W. Saenrang, R. Utke, *et al.*, Effect of hydrogen on magnetic properties in MgO studied by first-principles calculations and experiments, *Sci. Rep.*, 2022, **12**(1), 10063, DOI: **10.1038/s41598-022-13949-w**.

This journal is © the Partner Organisations 2025

*Inorg. Chem. Front.*, 2025, **12**, 342–354 | **353**

49 Y. Abe, K. Kato, M. Kawamura and K. Sasaki, Rhodium and Rhodium Oxide Thin Films Characterized by XPS, *Surf. Sci. Spectra*, 2002, **8**(2), 117–125, DOI: **10.1116/11.20010801**, (acccessed 10/7/2024).

50 R. Sui, J. Mantzaras and R. Bombach, H2 and CO heterogeneous kinetic coupling during combustion of H2/CO/O2/N2 mixtures over rhodium, *Combust. Flame*, 2019, **202**, 292–302, DOI: **10.1016/j.combustflame.2019.01.021**.

51 L. S. Kibis, A. I. Stadnichenko, S. V. Koscheev, V. I. Zaikovskii and A. I. Boronin, XPS Study of Nanostructured Rhodium Oxide Film Comprising Rh4+ Species, *J. Phys. Chem. C*, 2016, **120**(34), 19142–19150, DOI: **10.1021/acs.jpcc.6b05219**.

52 M. Akbayrak and A. M. Önal, High Durability and Electrocatalytic Activity Toward Hydrogen Evolution Reaction with Ultralow Rhodium Loading on Titania, *J. Electrochem. Soc.*, 2020, **167**(15), 156501, DOI: **10.1149/1945-7111/abb9cf**.

53 G. Wang, S. Jing and Y. Tan, Branched Pd@Rh core@shell nanocrystals with exposed Rh {100} facets: an effective electrocatalyst for hydrazine electro-oxidation, *Sci. Rep.*, 2017, **7**(1), 16465, DOI: **10.1038/s41598-017-16776-6**.

54 S. Nokbin, J. Limtrakul and K. Hermansson, DFT plane-wave calculations of the Rh/MgO(001) interface, *Surf. Sci.*, 2004, **566–568**, 977–982, DOI: **10.1016/j.susc.2004.06.039**.

55 L. Giordano, A. D. Vitto, G. Pacchioni and A. M. Ferrari, CO adsorption on Rh, Pd and Ag atoms deposited on the MgO surface: a comparative ab initio study, *Surf. Sci.*, 2003, **540**(1), 63–75, DOI: **10.1016/S0039-6028(03)00737-4**.

56 R. Pushpa, P. Ghosh, S. Narasimhan and S. de Gironcoli, Effective coordination as a predictor of adsorption energies: A model study of NO on Rh(100) and Rh/MgO(100) surfaces, *Phys. Rev. B:Condens. Matter Mater. Phys.*, 2009, **79**(16), 165406, DOI: **10.1103/PhysRevB.79.165406**.

57 S. Tang, Z. Zhang, L. Xu, H. Qin, J. Dong, Q. Lv, J. Han and F. Song, Ultrafine nickel-rhodium nanoparticles anchored on two-dimensional vanadium carbide for high performance hydrous hydrazine decomposition at mild conditions, *J. Colloid Interface Sci.*, 2024, **669**, 228–235, DOI: **10.1016/j.jcis.2024.04.204**.

58 M. Zahmakıran and S. Özkar, Metal nanoparticles in liquid phase catalysis; from recent advances to future goals, *Nanoscale*, 2011, **3**(9), 3462–3481, DOI: **10.1039/C1NR10201J**.

59 Z. Zhang, Z.-H. Lu, H. Tan, X. Chen and Q. Yao, CeOx-modified RhNi nanoparticles grown on rGO as highly efficient catalysts for complete hydrogen generation from hydrazine borane and hydrazine, *J. Mater. Chem. A*, 2015, **3**(46), 23520–23529, DOI: **10.1039/C5TA06197K**.

60 C. Li, Y. Dou, J. Liu, Y. Chen, S. He, M. Wei, D. G. Evans and X. Duan, Synthesis of supported Ni@(RhNi-alloy) nanocomposites as an efficient catalyst towards hydrogen generation from N2H4BH3, *Chem. Commun.*, 2013, **49**(85), 9992–9994, DOI: **10.1039/C3CC45697H**.

61 J. Chen, Z.-H. Lu, Q. Yao, G. Feng and Y. Luo, Complete dehydrogenation of N2H4BH3 with NiM-Cr2O3 (M = Pt, Rh, and Ir) hybrid nanoparticles, *J. Mater. Chem. A*, 2018, **6**(42), 20746–20752, DOI: **10.1039/C8TA08050J**.

62 K. M. Neyman, C. Inntam, A. V. Matveev, V. A. Nasluzov and N. Rösch, Single d-Metal Atoms on Fs and Fs+ Defects of MgO(001): A Theoretical Study across the Periodic Table, *J. Am. Chem. Soc.*, 2005, **127**(33), 11652–11660, DOI: **10.1021/ja052437i**.

63 H. Y. Wang and E. Ruckenstein, Partial Oxidation of Methane to Synthesis Gas over MgO- and SiO2-Supported Rhodium Catalysts, *J. Catal.*, 1999, **186**(1), 181–187, DOI: **10.1006/jcat.1999.2535**.

64 H. Tanaka, R. Kaino, K. Okumura, T. Kizuka, Y. Nakagawa and K. Tomishige, Comparative study of Rh/MgO modified with Fe, Co or Ni for the catalytic partial oxidation of methane at short contact time. Part I: Characterization of catalysts, *Appl. Catal., A*, 2010, **378**(2), 175–186, DOI: **10.1016/j.apcata.2010.02.017**.

65 R. A. Lai, T. M. Hymel, V. K. Narasimhan and Y. Cui, Schottky Barrier Catalysis Mechanism in Metal-Assisted Chemical Etching of Silicon, *ACS Appl. Mater. Interfaces*, 2016, **8**(14), 8875–8879, DOI: **10.1021/acsami.6b01020**.

66 H. Hosono and M. Kitano, Advances in Materials and Applications of Inorganic Electrides, *Chem. Rev.*, 2021, **121**(5), 3121–3185, DOI: **10.1021/acs.chemrev.0c01071**.

67 J. Hölzl and F. K. Schulte, in *Work function of metals. In Solid Surface Physics*, ed. J. Hölzl, F. K. Schulte and H. Wagner, Springer, Berlin, Heidelberg, 1979, pp. 1–150.

68 H. Hosono, Electron Transfer from Support/Promotor to Metal Catalyst: Requirements for Effective Support, *Catal. Lett.*, 2022, **152**(2), 307–314, DOI: **10.1007/s10562-021-03648-y**.

69 G. Pacchioni, Oxygen vacancy: The invisible agent on oxide surfaces, *ChemPhysChem*, 2003, **4**(10), 1041–1047, DOI: **10.1002/cphc.200300835**.

70 P. V. Sushko, A. L. Shluger and C. R. A. Catlow, Relative energies of surface and defect states: ab initio calculations for the MgO (001) surface, *Surf. Sci.*, 2000, **450**(3), 153–170, DOI: **10.1016/S0039-6028(00)00290-9**.

**354** | *Inorg. Chem. Front.*, 2025, **12**, 342–354

This journal is © the Partner Organisations 2025